Electromechanical properties of sodium bismuth titanate thin films

Stephania Kossman, Arthur Hamieh, Freddy Ponchel, Denis Remiens, Maxence Bigerelle

Electromechanical properties of sodium bismuth titanate thin films

Stephania Kossman [a,*], Arthur Hamieh [b], Freddy Ponchel [b], Denis Rémiens [b], Maxence Bigerelle [a]

[a] Laboratoire d'Automatique, de Mécanique et d'Informatique Industrielles et Humaines, LAMIH UMR CNRS 8201, Université Polytechnique Hauts-de-France, 59300 Valenciennes, France
[b] IEMN-DOAE UMR CNRS 8520, Université Polytechnique Hauts-de-France, 59300 Valenciennes, France

ARTICLE INFO

Keywords:
Lead free piezoelectric films
Sputtering
Crystallization
Electromechanical characterization
Nanoindentation

ABSTRACT

Lead-free piezoelectric sodium bismuth titanate (BNT) films are promising candidates for actuators applications as an alternative to lead zirconate titanate films. We focused in this work on the growth and characteristics of BNT films deposited by sputtering on silicon substrates with $LaNiO_3$ electrodes. The films are amorphous previous to post-annealing treatments. We studied the influence of the crystallization state and film thickness on their electromechanical properties. Namely, we evaluated the piezoelectric properties, reduced elastic modulus, and hardness. BNT films fully crystallized (f-c) in the desired perovskite structure, without second phase, after post-annealing at 650°C. Relative permittivity grew from 60 to 540 for an amorphous vs. a f-c film and the d_{33eff} coefficient improved with film thickness to 60 pm/V for a 450 nm thick film. The BNT film's mechanical properties increased with film crystallization from the amorphous structure to the f-c: 134 to 149 GPa for reduced modulus and 7 to 9 GPa for hardness. However, the film thickness did not remarkably modify the mechanical properties, yet a slight decrease for the 450 nm film was explained by previous cracking on the surface.

1. Introduction

Piezoelectricity is an electromechanical intrinsic property of some materials, which consists of the bidirectional conversion of mechanical energy into electrical energy. Piezoelectric materials (bulk and thin films) have multiple applications such as accelerometers, transducers, frequential filters, microphones, gyroscopes, nano or micro-electromechanical systems (NEMS and MEMS), etc. [1–3].

One of the most largely used piezoelectric materials is the solid solution lead zirconate titanate (PZT), which crystallizes in a perovskite structure. This solid solution has outstanding piezoelectric properties associated with a weak coercive field, making this material a reference in the field since its discovery in the fifties'. The presence of lead in PZT materials' composition produces many health and environmental problems. Namely, the disposal of electronic devices at the end of their service life and the manufacture of new devices containing hazardous substances are part of several restrictions within the European Union [4, 5]. Therefore, the development of lead-free piezoelectric materials is on the urge.

Research in lead-free piezoelectric materials has existed since decades ago. However, recently it has significantly increased for bulk and thin-film materials [6]. There are two emerging candidates among the lead-free piezoelectric family's materials, potassium sodium niobate and sodium bismuth titanate (BNT or NTB).

In this work, we have focused in the study of BNT films since their understanding (synthesis and behavior) are still under development, mainly due to challenges to achieve a precise stoichiometry control to obtain the perovskite structure [7,8], despite that the BNT bulk form has been largely studied [9–13]. BNT films present advantageous piezoelectric properties (d_{33} = 40-80 pm/V) [14–17], these values will still improve with the many works currently being carried out on lead-free piezoelectric materials. There are many application regarding the inverse piezoelectric effect such as actuators, representing an excellent alternative for temperatures under 150°C [18].

The mechanical characterization of piezoelectric films is necessary to further comprehend its electromechanical piezoelectrical behavior, given the relationship between mechanical and electrical energy conversion in these materials. Nanoindentation is a broadly used technique in the mechanical characterization of thin films since it solicits small volumes. Previous works have studied the mechanical properties of piezoelectric films by nanoindentation typically addressing two main variables, composition and temperature, for example, $(Na_{1-x}K_x)_{0.5}Bi_{0.5}TiO_3$ films as a function of the potassium content [18]; Nb-doped $(Na_{0.85}K_{0.15})_{0.5}Bi_{0.5}Ti_{(1-x)}Nb\ xO_3$ films as a function of niobium

* Corresponding author.
E-mail address: stephaniakossman@gmail.com (S. Kossman).

content [19]; $(Bi_{0.5}Na_{0.5})TiO_3$–$(Bi_{0.5}K_{0.5})TiO_3$–$BaTiO_3$ films as a function of the annealing temperature [20]; PZT films versus testing temperature [21].

The current study presents the effects of the annealing temperature, film thickness, stacking layers of the substrate, and their impact on the structural and electromechanical properties of BNT films. Mechanical characterization of BNT films was studied by nanoindentation.

2. Materials and methods

2.1. Films deposition

LNO and BNT films were deposited by radio frequency (RF) magnetron sputtering (Plassys MP600). First, the bottom electrode, $LaNiO_3$ (LNO), was sputtered on a silicon substrate heated at 450°C in plasma of Ar:O_2 = 4:1 using a 76.2 mm (3") ceramic target, 10 Pa pressure, and 3 nm/min deposition rate. After deposition, the LNO-200 nm thick films were systematically annealed in air at 700°C during one hour to improve their electrical conductivity [22]. In addition, stoichiometric BNT films were grown on LNO/Si substrate (or LNO/SiO_2/Si for some tests), using a homemade target fabricated by cold pressure of mixed oxide powders (Bi_2O_3, $Na_2Ti_3O_7$, and TiO_2) with high purity (>99.99%). BNT thin films were sputtered on LNO buffered substrates in pure Ar gas at 1.3 Pa pressure and 100 W RF power. Substrates were fixed at a distance of 8 cm from the target and heated at 200°C. The choice of this temperature allows to control Bi concentration in the film. This temperature is well below the crystallization temperature of BNT. It is therefore an ex-situ process (growth of an amorphous film) and post-deposition annealing is necessary to crystallize the film at the perovskite phase (as discussed in our previous work [8]). BNT films were deposited for different deposition times at 2.5 nm/min deposition rate to vary the film thickness (t): 220, 350, and 450 nm. After deposition, the as-deposited films were amorphous. To obtain partially and fully crystallized films, respectively, different post-annealing treatments were systematically performed in air at 450°C and 650°C for one hour.

Table 1 summarizes the nomenclature used in this work, the configuration of each sample (substrate stacking layers and film thickness), and the crystallization rate of the films according to the post-annealing treatment. Fig. 1-a shows the structure of the tested samples.

2.2. Crystallographic, morphological, and electrical characterization

The crystallographic structures of LNO and BNT were analyzed by X-ray diffraction (XRD) using Cu K_α radiation with a Rigaku smartlab diffractometer (θ - 2 θ configuration). The microstructure was observed by scanning electron microscopy (SEM) with JEOL JSM-IT100 used at low voltage (5 kV). BNT film thickness was measured by Veeco Dektak 150 profilometer and SEM.

To measure the electrical properties, Pt top electrodes (Ø 100 to 200 μm) were deposited on BNT films by lift-off process (Fig. 1-b). Relative dielectric constant was measured at 10 kHz frequency using a HP4192A impedance analyzer. Piezoelectric response was studied using a homemade system based on a laser Doppler vibrometer. Specifically, the d_{33eff} piezoelectric coefficient was measured by a single beam method, namely

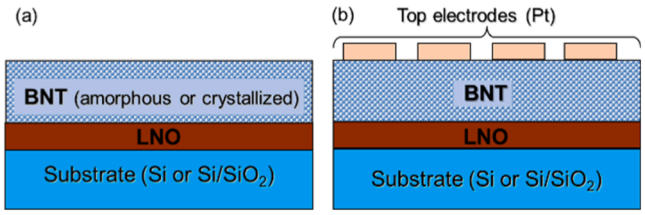

Fig. 1. BNT sample configuration for mechanical properties evaluations; b) BNT structure for electrical measurements (presence of Pt top electrodes)

a V_{AC} voltage is applied on the sample (V_{AC} = 1 V) and a V_{DC} is superimposed. The measurement frequency is fixed at 10 kHz. The tested sample (substrate + film) is well clamped (to suppress the bending effect of the substrate). A detailed description of this method is reported by Herdier *et al.* [23] and Pokorny *et al.* [24].

2.3. Mechanical characterization

Mechanical characterization of unpoled BNT films were performed through nanoindentation tests, using a TriboIndenter TI-980 (Hysitron, Bruker, Minneapolis, MN, USA), operating under the mode of ultrahigh-speed mechanical property mapping (XPM). We also evaluated the mechanical properties of the LNO (bottom electrode) and Si (substrate).

We used a Berkovich diamond tip for all the tests, its area function was calibrated in fused quartz [25,26], obtaining valid results starting at 18 nm of penetration depth (setting six coefficients for the area function). Tests were performed at two maximum loads, 250 and 500 μN, which corresponded to an approximately maximum penetration depth of 10 % and 20 % (at 500 μN) for the thicker (450 nm) and thinner film (220 nm), respectively. These loads were selected in order to avoid the influence of the underneath layers in the mechanical properties of the BNT films, further explanations are given in the results Section 3.3.3.

At least 400 tests were performed per sample, in arrays of 10 × 10 with 1 μm (at 250 μN) and 2 μm (at 500 μN) spacing between indents, and 50 μm spacing between arrays. The tests were performed at a lateral move speed of 10μm/s, a setpoint load of 1 μN, and load, hold, and unload times equal to 0.2 s; the data acquisition was configured to 2000 points/s and the piezo translation protocol was set to serpentine mode.

The reduced elastic modulus and indentation hardness were calculated by Eq. (1) and (3). Only the reduced elastic modulus was calculated since the Poisson's ratio of the BNT films has not been reported elsewhere.

Table 2
Comparison aspects for the nanoindentation characterization of BNT films.

Aspect	Samples
(i) Crystallization	3 BNT films of the same thickness (450 nm): fully crystallized, partially crystallized, and amorphous
(ii) Substrate (stacking layers)	2 BNT films of the same thickness (350 nm) deposited in LNO/SiO_2/Si and LNO/Si substrates
(iii) Film thickness	3 BNT films of 3 thicknesses: 220, 350 and 450 nm

Table 1
BNT films and substrates samples characteristics.

Nomenclature	Substrate stacking	Film thickness (t) (nm)	Deposition rate (nm/min)	Film crystallization	Post-annealing treatment
BNTA	LNO/Si	450	2.5	f-C	650°C/ 1 h
BNTB	LNO/Si	350	2.5	f-C	650°C/ 1 h
BNTC	LNO/SiO_2/Si	220	2.5	f-C	650°C/ 1 h
BNTD	LNO/SiO_2/Si	350	2.5	f-C	650°C/ 1 h
BNTE	LNO/Si	450	2.5	A	N/A
BNTF	LNO/SiO_2/Si	450	2.5	p-C	450°C/ 1 h
LNO	Si	200	3.0	f-C	700°C/ 1 h

f-C: fully-crystallized, p-C: partially-crystallized, A: amorphous.

We considered three aspects described in Table 2 to study the mechanical properties by nanoindentation of the BNT films. More precisely the state of crystallization (full, partial or amorphous film), the film thickness, and the presence of a silicon oxide layer located between the Si substrate and the LNO electrode.

In addition, in-situ (in the nanoindentation instrument) topographical measurements were performed by scanning probe microscopy (SPM) using a Berkovich tip covering areas of $6 \times 6\ \mu m^2$ in each sample.

2.3.1. Calculation of mechanical properties by nanoindentation

The calculation of the mechanical properties (elastic modulus and hardness) through nanoindentation tests depends on three measures identified from the load-displacement (*P-h*) curve: the maximum displacement and load (h_{max} and P_{max}) and the contact stiffness (*S*). h_{max} and P_{max} are directly determined from the *P-h* curve. Contact stiffness is estimated by approximating the unloading curve to a power law [26], and then its derivative (dP/dh) is evaluated at h_{max} to obtain S.

Then, the elastic modulus and hardness are computed according to the following relationships [26].

$$E_r = \frac{S\sqrt{\pi}}{2\beta\sqrt{A_c}} \tag{1}$$

$$\frac{1}{E_r} = \frac{(1-\nu^2)}{E} + \frac{\left(1-\nu_i^2\right)}{E_i} \tag{2}$$

$$H = \frac{P_{max}}{A_c} \tag{3}$$

where E_r is the reduced elastic modulus; β is a geometrical factor accounting for radial displacements (1.034); A_c is the contact area; E, ν and E_i, ν_i are the elastic modulus and Poisson's ratio of the material and indenter respectively.

The next expressions describe the contact area and contact depth [26].

$$A_c = C_0 h_c^2 + C_1 h^2 + C_2 h^{1/2} + C_3 h^{1/4} + \ldots + C_8 h^{128} \tag{4}$$

$$h_c = h_{max} - \varepsilon \frac{P_{max}}{S} \tag{5}$$

where C_n are constants obtained by the calibration performed in a reference material (e.g., fused quartz). ε is a constant depending on the geometry of the indenter (0.75 for Berkovich indenter).

3. Results and discussion

3.1. BNT films crystallography and microstructure

Fig. 2 presents the XRD patterns of BNT films after deposition and annealing at different temperatures, 450°C and 650°C. The XRD pattern of the as-deposited film shows only peaks corresponding to LNO, indicating that the BNT film is amorphous. However, for films annealed at 450°C and 650°C, the XRD patterns display BNT and LNO peaks, mainly distinguished at 2-theta about 46-47°; the occurrence of BNT peaks signify that BNT films crystallized in perovskite structure with a (100) orientation. This crystallization is enhanced by the structure matching between BNT and LNO. Besides, the intensity of the BNT peaks increases while increasing the annealing temperature (Fig. 2). Hamieh et al. showed that BNT film begins to crystallize from an annealing temperature of 400°C and that crystallization rises with increasing temperature to reach a maximum of crystallization at 650°C [8]. It is worth mentioning that the peak at approximately 2-theta = 33° corresponds to the signal of the Si substrate, which is highly sensitive of the measurement conditions [27], explaining why this peak appeared systematically in Fig. 2.

XRD patterns of BNT films with different thicknesses: 220, 350, and 450 nm are represented in Fig. 3. All patterns exhibit (h00) peaks corresponding to the BNT compound, evidencing a highly oriented growth. In addition, the intensity of BNT peaks increases with thickness, which was expected as the peak intensity is proportional to the film thickness. Furthermore, we observed a slight shift in the (h00) peaks to lower angles as the thickness increased from 220 to 450 nm. This leftward shift of BNT peaks suggests the existence of residual tensile stresses in the film that partially relax when increasing thickness. Ion *et al.* [28] associated this effect with a gradual relaxation of the substrate effect, pertaining to misfit and clamping.

Fig. 4 shows the cross-section and surface SEM images of the 450 nm thickness BNT film annealed at 650°C (fully crystallized). The film exhibits a dense structure with a granular microstructure (grain size is approximately 400 nm), indicating a good film crystallization after the post-annealing treatment at 650°C. All the films present the same microstructure despite their thickness. However, only the film of 450 nm thickness presented cracks, as shown in Fig. 4-b.

3.2. Electric properties

The dielectric properties of as-deposited and annealed films are shown in Table 3, the films present the same thickness ($t = 450$ nm). The as-deposited film (amorphous structure) exhibited a relative

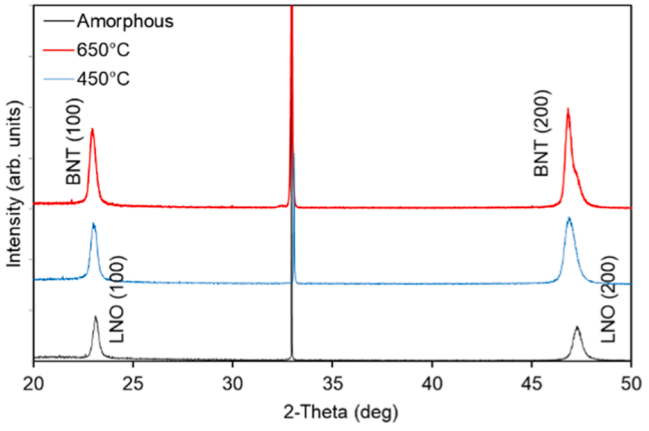

Fig. 2. XRD patterns of BNT films after deposition and annealing at different 450°C and 650°C.

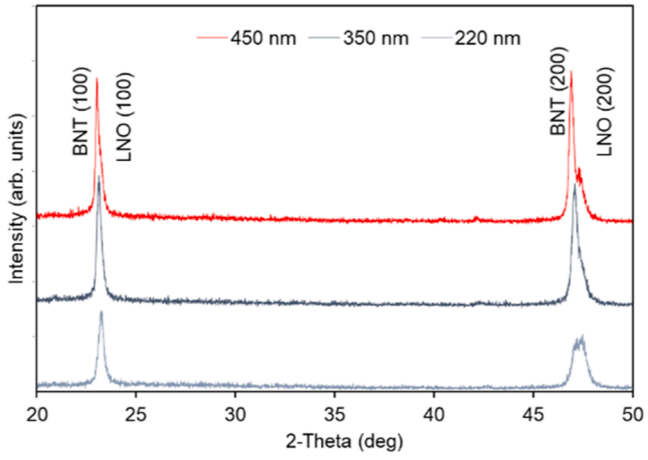

Fig. 3. XRD patterns of BNT films with different thicknesses: 220 nm, 350 nm, and 450 nm.

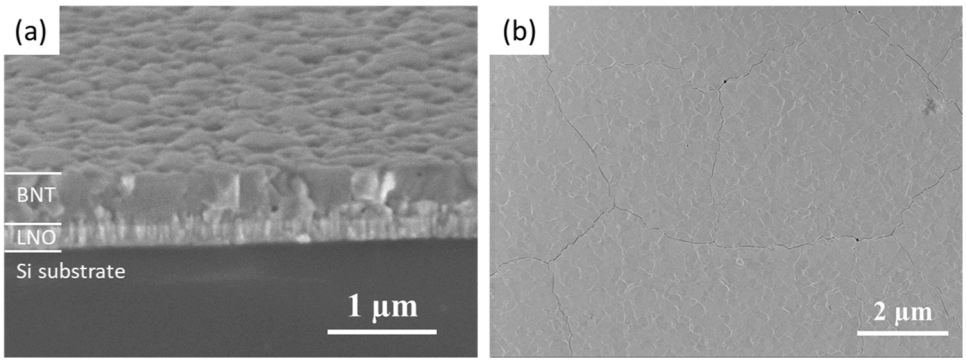

Fig. 4. SEM images in secondary electrons mode (5 kV) of the cross-section (a) and the surface (b) of 450 nm thick BNT film annealed at 650°C.

Table 3
Dielectric properties of BNT films (t=450 nm) in the as-deposited and annealed state.

Film	A	p-C	f-C
Permittivity	60	220	540

permittivity of 60. In contrast, the annealed films (f-C and p-C) presented higher relative permittivity values of 220 and 540 for annealing temperatures of 450°C and 650°C, respectively. These results indicate, as expected, that relative permittivity values are affected by the structural properties presented in the previous section, namely, amorphous films exhibit low permittivity compared to the fully crystallized film, annealed at 650°C. The intermediate permittivity value for the film annealed at 450°C confirmed the coexistence of amorphous and crystallized phases in the film.

Piezoelectricity of f-C BNT films was evaluated by coefficient d_{33eff}, a suitable indicator for actuator applications. Fig. 5 shows the variation of this coefficient as a function of film thickness.

The coercive field varies with the film thickness, it is of the order of 70 kV/cm for a 450 nm thick film. Also, the piezoelectric coefficient d_{33eff} increase with the growth of film thickness, reaching 60 pm/V at 450 nm. This behavior is completely normal. Namely, for very thin films, the interface effects dominate the response; beyond certain thickness the actual piezoelectric response of the film is measured. These effects are well described in the reference [29]. Hence, the increase in the film thickness approaches the piezoelectric constant to the free film value.

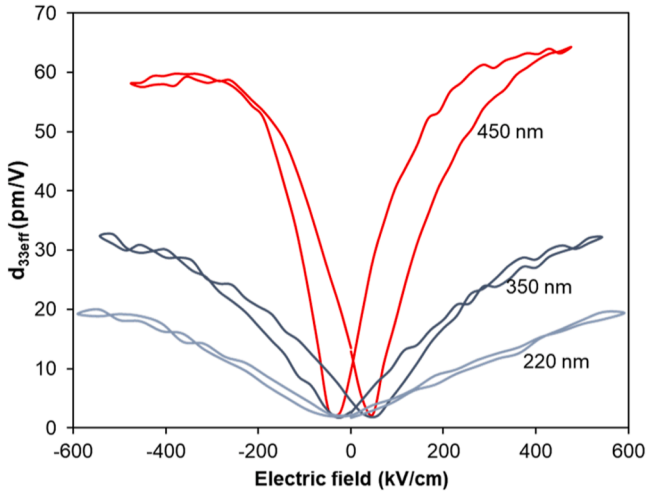

Fig. 5. Evolution of d_{33eff} piezoelectric coefficient as a function of applied electric field for f-C BNT films with various thicknesses.

3.3. *Mechanical characterization by nanoindentation*

Table 4 summarizes the mechanical properties (reduced modulus and hardness) of the BNT films, LNO bottom electrode film, and Si substrate estimated by nanoindentation tests.

Table 4 reports the mean, standard deviation, and 95% confidence interval values for hardness and reduced modulus. The standard deviation represents the dispersion among the values, and the 95% confidence interval estimates the true mean of the population with a 95% accuracy. These two values represent the stochastic part of the uncertainty in the nanoindentation measurements. Further discussion is given in the following sections.

It is worth mentioning that some load-displacement curves corresponding to the BNT films exhibit pop-in events and slope changes. Pop-in events are typically described as displacement bursts in load-control nanoindentation tests [30,31], as illustrated in Fig. 6. These curves were excluded from the mechanical properties' calculation reported in Table 4. We only use the curves showing a regular load-displacement path to calculate the mechanical properties since pop-in events can drastically modify the maximum displacement, leading to the miscalculation of the contact area and, therefore, the mechanical properties. The load-displacement curves (with and without pop-in) were classified through a convolutional neural network model described elsewhere [32] with about 92% accuracy; the percentage of curves presenting pop-in are given in Table 4.

The mechanical properties of the LNO (100) film are reported in Table 4. The estimated reduced modulus agrees with Young's modulus values reported for LNO bulk ceramic [33]. These authors [33] obtained Young's modulus values of 192 to 198 GPa, according to the crystallization phase (rhombohedral or monoclinic) with similar polycrystalline behavior. Hardness results obtained by nanoindentation are two times bigger than the bulk material, which could be related to the different scales of measurement.

Surface roughness of the BNT films was obtained by in-situ SPM measurements and quantified by the surface roughness parameter Sa (arithmetical mean height of a surface) represented in Fig. 7. The results revealed two principal aspects. First, the parameter Sa slightly increases with the increase of the film thickness from approximately 3.0 to 1.5 nm. Second, surface roughness increases with the film crystallization. That is, the fully crystallized film presented a more significant roughness (about 3.0 nm for f-c vs. 1.8 nm for the amorphous film). In addition, LNO/Si bottom electrode presented a smaller Sa value of about 1.3 nm. Similar results were obtained through AFM characterizations in the BNTA film. These results highlight the fact that surface roughness of amorphous film follows the smooth surface of the substrate. On the other hand, when the film is fully crystallized the existence of grains and grain boundaries increase the surface roughness.

Table 4
Mechanical properties measured by nanoindentation testing.

Sample	Thickness (nm)	P_{max} (μN)	Count	*Er* (GPa)			*H* (GPa)			Pop-in %
				mean	SD	95% CI	mean	SD	95% CI	
BNTA	450	250	192	149	14	1.9	9.0	1.3	0.19	52
		500	222	136	11	1.4	7.7	1.0	0.13	45
BNTB	350	250	179	152	13	2.0	9.9	1.5	0.22	11
		500	351	143	10	1.1	8.2	1.0	0.11	12
BNTC	220	250	260	146	9	1.1	9.1	1.0	0.13	13
		500	390	137	6	0.6	8.3	0.7	0.07	3
BNTD	350	250	185	151	11	1.6	9.6	1.2	0.17	8
		500	374	139	8	0.8	8.5	1.0	0.10	7
BNTF	450	250	584	134	12	1.0	7.4	1.2	0.10	3
		500	591	129	10	0.8	6.8	1.2	0.10	2
BNTE	450	250	187	123	8	1.1	6.3	0.8	0.12	7
		500	271	120	8	1.0	6.0	1.0	0.11	10
LNO		250	189	174	18	2.6	12.1	2.2	0.31	6
		500	199	167	14	1.9	12.5	2.0	0.27	1
Si		250	200	167	5	0.7	11.3	0.3	0.04	0
		500	200	159	4	0.5	10.7	0.3	0.04	0

SD: standard deviation; 95% CI: 95% confidence interval = 1.96 x standard error. Count: number of tests. Pop-in %: percentage of curves that showed pop-in.

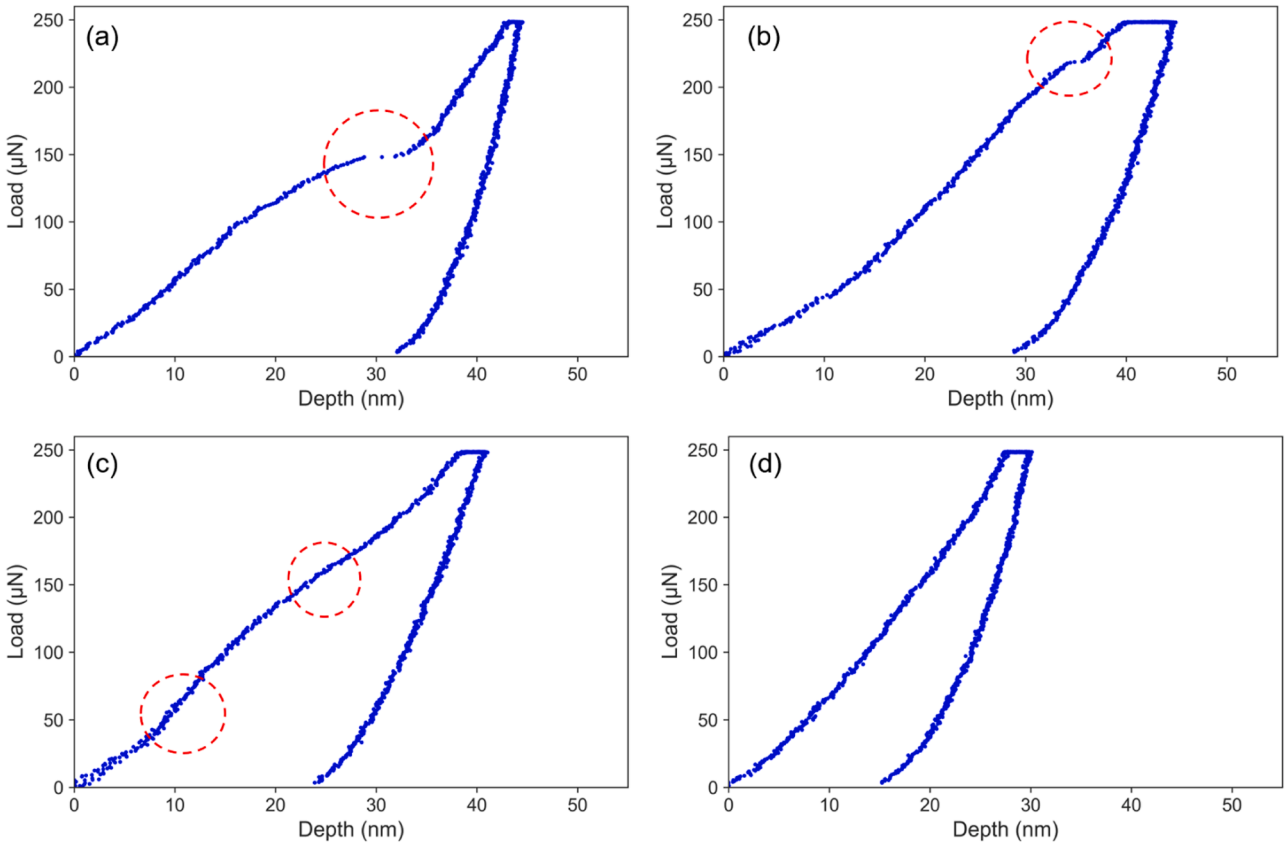

Fig. 6. Load-displacement P-h curves obtained by nanoindentation tests on BNT films presenting different characteristics: (a) – (b) pop-ins, (c) slope changes, and (d) regular loading-unloading path.

3.3.1. Influence of crystallization rate in the mechanical properties of BNT films

Fig. 8 shows the variation of modulus and hardness of BNT films according to their crystallization state. These results put evidence that the film crystallization directly modifies the mechanical properties of the BNT films. For fully crystallized films, both mechanical properties increased. The full amorphous film presented a reduction of modulus and hardness values of about 19 % and 34 %, respectively, compared to the fully crystallized film. The partially crystallized film displayed a smaller drop of approximately 13 % and 24 % for the modulus and hardness.

In addition, modulus and hardness values decreased with the increase of the applied load. This response partially corresponds to an effect of the surface roughness as already reported elsewhere [34,35]. Despite the small Sa roughness values (below 3 nm, Fig. 7), the scale of measurement of our nanoindentation tests was about 20 nm at 250 μN and 40 nm at 500 μN. According to the standard ISO 1477-1 [36], the penetration depth should be twenty times the surface roughness (Ra, equivalent parameter to Sa), that is about 60 nm of penetration depth, suggesting that measurements at 250 μN were potentially affected by the surface topography due to calculation of the contact area. This effect should be less significant 500 μN due to the increase in the contact

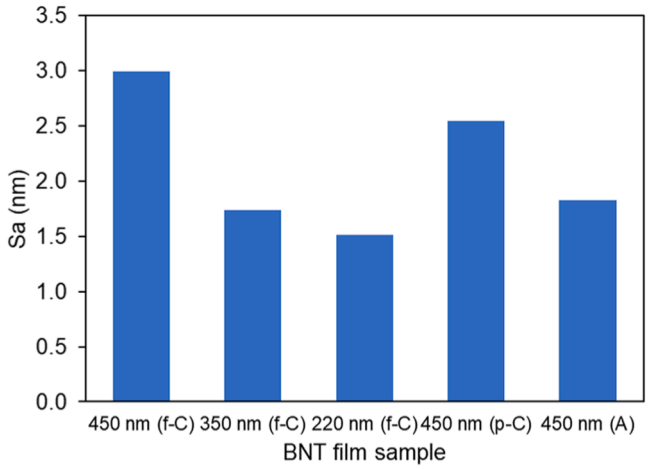

Fig. 7. Sa roughness parameter values for BNT film according to their thickness and crystallization. Roughness measurements were performed by SPM (6 μm x 6 μm area) using a Berkovich diamond tip.

depth. Fig. 9 illustrates the topography of the 450 nm thick BNT film that evidences why the nanoindentation results are affected by the surface roughness. Moreover, it is worth mentioning that the tip area calibration was valid in our experiments from 18 nm; nevertheless, it is well known that tip area calibration carries uncertainties [37], which affect our measurements, especially at the small penetration depth where the tip area coefficients are pretty relevant.

In Fig. 8, we can notice that the drop of the mechanical properties with the load is more predominant with the film crystallization. For the reduced modulus, we obtained a drop of 9%, 4%, and 2 % for BNTA (f-C), BNTF (p-C), and BNTE (A) films, respectively. Hardness values showed a more considerable reduction, 15%, 7%, and 5% for BNTA, BNTF, and BNTE films, respectively. These results suggest that the film crystallization modifies the top surface characteristics of the BNT films. This could be partly explained by the surface roughness measurements (Sa, Fig. 7); specifically, for the fully crystallized film, the Sa parameter was about two times bigger than the amorphous film of the same thickness.

3.3.2. *Influence of staking layers in the reduced modulus and hardness of BNT films*

The mechanical properties of BNTB and BNTD films of the same thickness (350 nm) deposited in the two different staking substrate systems, LNO/SiO_2/Si and LNO/ Si, presented similar values (Table 4). Two t-tests (modulus and hardness data) were conducted between both samples to determine if the values were statistically different. The statistical t-test considers the mean values associated with their confidence interval. The resulting p-values were 2.37×10^{-5} and 8.79×10^{-2} for modulus and hardness, correspondingly. According to these results, the mean values of the modulus are statistically different (p-value < 0.05), in contrast to hardness values that are not statistically different (p-value > 0.05). Despite the statistical difference between modulus values, the mean properties present a variation inferior to 3 %, mainly within the 10 % typical uncertainty of nanoindentation tests [36,38]. Thus, indicating that both coatings exhibit comparable properties. Uncertainties in

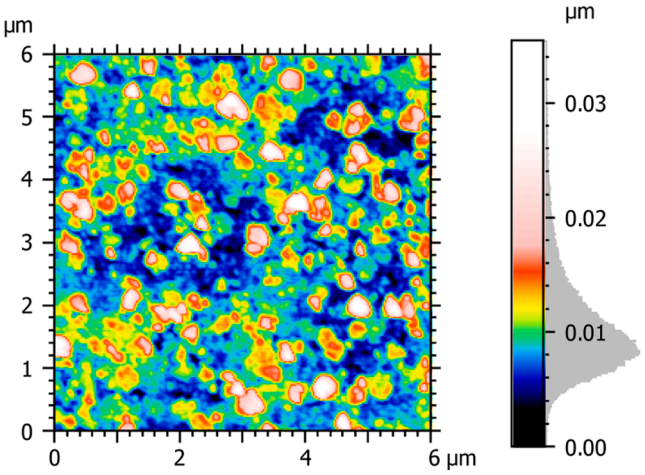

Fig. 9. 2D topography representation of f-c BNT film (t=450 nm). The topography was obtained by SPM (6 μm x 6 μm area) using a Berkovich diamond tip.

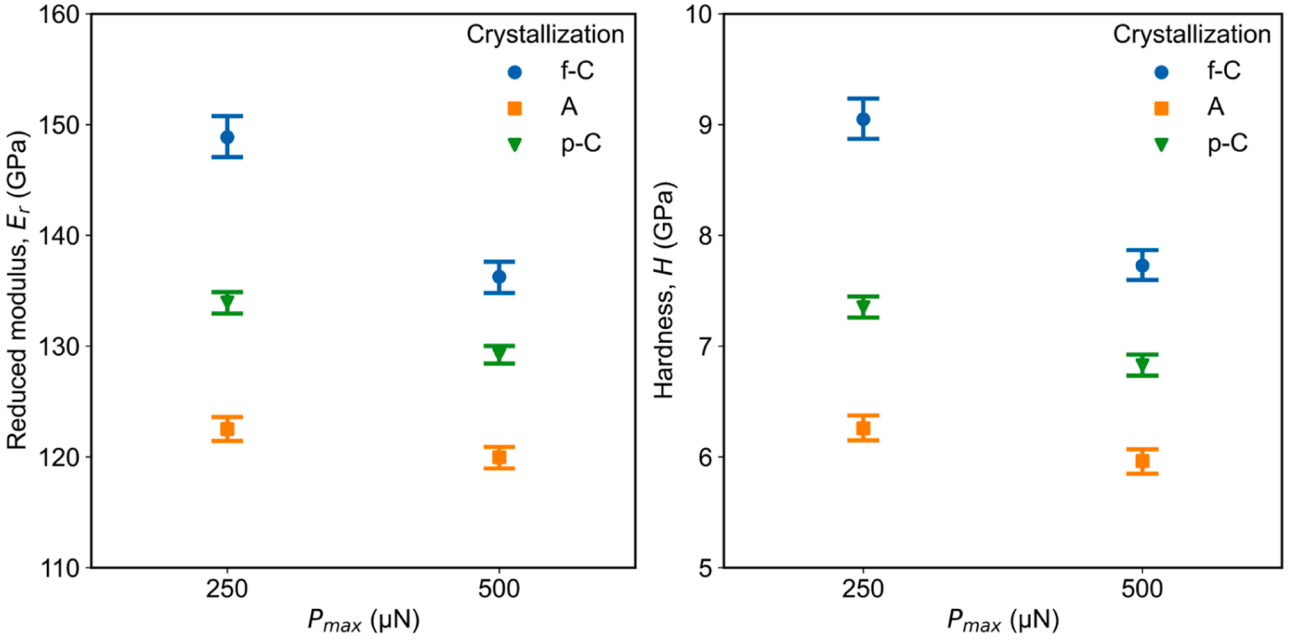

Fig. 8. Reduced elastic modulus and hardness variation vs. the maximum load for different crystallization fully crystallized (f-C), partially crystallized (p-C), and amorphous (A) for films of thickness=450 nm (BNTA, BNTF, and BNTE).

nanoindentation tests are related to many sources such as system noise, environmental conditions, indenter geometry, surface state, etc. [39].

These results indicated that at the penetration depths at which the mechanical properties were estimated (< 38 nm), the stacking layers of the substrate did not seem to have a significant influence.

3.3.3. *Influence of the BNT films thickness in the reduced elastic modulus and hardness*

Fig. 10 illustrates hardness and reduced modulus according to the film thickness variation at both tested loads. BNTB and BNTD films (Section 3.3.2) give results corresponding to the thickness of 350 nm.

Hardness and reduced modulus results showed a similar trend with increased film thickness. Both properties decrease with the applied maximum load. This reduction at the studied penetration depths is not a response of the underneath layer, LNO, which had a higher modulus and hardness (Table 4). This response probably corresponds to a consequence of the surface roughness, as previously mentioned in Section 3.3.1.

Variation of the reduced modulus and hardness with the film thickness at the same applied load is smaller than the characteristic uncertainty of 10 % for nanoindentation tests, indicating that the films exhibit a comparable local mechanical property regardless of their thickness. Nonetheless, the slightly reduction of both mechanical properties (< 4 % for *Er* and < 9 % for *H*) for the thicker BNT film could be related the cracks observed on the surface (Fig. 4), and by consequence, to the film relaxation [18,28].

It is essential to highlight that the estimated properties correspond to the BNT intrinsic properties and not to a composite response affected by the underneath substrate. Thus, both mechanical properties showed a diminution with the increase of the penetration depth. Indicating that the harder and stiffer LNO film did not influence the mechanical response at the testing penetration depths [40].

In addition, two factors reduced the uncertainty of the estimated mechanical properties. First, the important number of tests performed per sample (at least 200 per load), leading to the statistical significance of our results. Second, the representative testing areas (minimum 20 × 20 μm^2), since the grain size of the BNT films was about 400 nm, thus, the tested zones were large enough to exhibit a representative behavior of the film.

The estimated reduced modulus values for the BNT films are within the order of magnitude of previously reported works. Dittmer et al. [9] determined Young's modulus of BNT bulk ceramic by impulse excitation technique obtaining 100 GPa at room temperature. Also, Ayrikyan et al. [41] studied ceramic/ceramic multilayer composite structures based on BNKT-6BA and BNT-7 BT ceramics by nanoindentation, obtaining elastic modulus values between 160 and 120 GPa. For clarification, the values reported in the present work correspond to the reduced modulus, which does not consider Poisson's ratio of the BNT film. In the study of Dittmer [9], Poisson's ratio was determined by an approximation related to the used impulse excitation technique. Poisson's ratio of BNT films is difficult to characterize due to the well-known complex anisotropy of the perovskite material [42].

Nevertheless, another study [43] on PZT films reported an increase of Young's modulus in comparison to the bulk PZT, which corroborates our results. In addition, a simple calculation of the elastic modulus considering a Poisson's ratio range between -0.5 to 0.5 (Fig. 11) generates higher values than the reference for the bulk BNT (100 GPa),

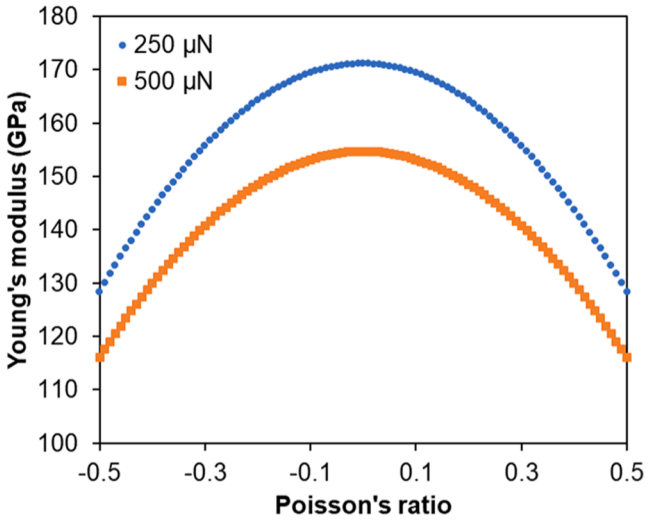

Fig. 11. Evolution of Young's modulus of BNT films as a function of the Poisson's ratio.

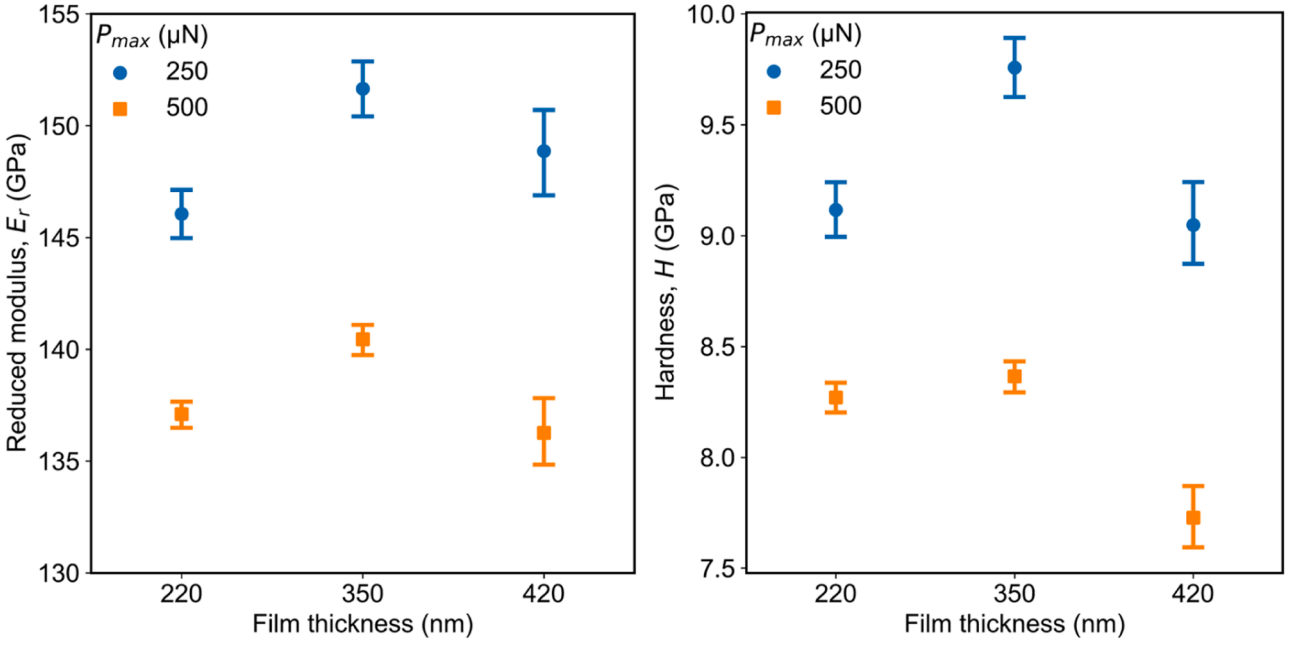

Fig. 10. Reduced modulus and hardness of f-C BNT films as a function of film thickness. The error bars represent the 95% confidence interval.

indicating that the elastic modulus of the BNT films is likely bigger than the values reported for the bulk ceramic.

3.3.4. *Pop-in events in nanoindentation curves of BNT films*

Pop-in events and slope changes in nanoindentation curves have been observed in piezoelectric films before [19,20,44]. These events are related to various causes such as incipient plasticity, dislocation nucleation [31,45], interaction of dislocations with a grain boundaries [31, 46], phase transformation [47], cracking [48,49]. Delobelle et al. [44] reported pop-in bursts in PZT films due to microcracking during nanoindentation tests. However, any evidence of microcracking due to nanoindentation was observed in the studied BNT films, highlighting that the loads used in this study were smaller than in the cited work. Instead, pop-in events in BNT films can be related to dislocation activation (nucleation, multiplication, and motion) [50,51]. Fang et al. [50] indicated that purely dislocation plasticity dominates during the indentation pop-in at small loads (e.g., 100 μN) when using Berkovich diamond tip (small radius tip) in $SrTiO_3$ oxide a perovskite prototype.

The higher percentage of detected pop-in events in the BNTA film (t= 450 nm) can be attributed to the increasing size and density of dislocations with the growth of thicker films. Namely, dislocations nucleation can start growing at larger thicknesses [52]. This hypothesis is coherent with the supposition that pop-ins events in the BNT films can be mainly related to dislocations activation. Another source of the higher pop-in percentage in the BNTA film can be cracks' preexistence, as shown in Fig. 4.

Regarding pop-in occurrence for films of the same thickness (450 nm) presenting different structures (A, f-C, and p-C). We observed that pop-in events increase in the fully crystallized film with respect to the two others having a total and partial amorphous structure, suggesting that pop-in appearance in nanoindentation curves of BNT films was mainly related to dislocation mechanisms.

4. Conclusions

We studied the influence of film crystallization and thickness on the BNT film properties like structural, microstructural, electrical and mechanical. We specially focus in the mechanical properties due to the lack of literature in the subject.

Amorphous BNT film (as-deposited) were transformed by annealing treatment to partially crystallized at 450°C or fully crystallized film at 650°C (without second phase), corroborated by XRD patterns. The as-deposited film diffractogram only revealed the signal of the LNO bottom electrode.

BNT f-C films exhibit a dense and granular microstructure. Yet, film cracking appears in the surface when increasing film thickness from 220 to 450 nm explained by the relaxation of residual stresses, corroborated by the leftward shift of the BNT peaks in the XRD diffractogram.

Dielectric properties, namely, relative permittivity showed a significant rise between the amorphous and the f-C film, from 60 to 540. Logically, the p-C film presented intermediate properties between these two states. In addition, piezoelectric properties, specifically the d_{33eff} coefficient, improve while increasing film thickness.

The implemented nanoindentation methodology represented a suitable technique to obtain the intrinsic mechanical properties (hardness and reduced modulus) of BNT films, our results were comparable with previous studies for the bulk version of this material. The reduced modulus and hardness were approximately 150 and 9 GPa, respectively. Nevertheless, both properties decreased for the partially crystallize and amorphous film. In addition, neither the stacking layers of the substrate nor the film thickness seems to significantly affect the mechanical properties. Though, a small diminution for the 450 nm thick film could be related to preexistent cracks.

Surface roughness of BNT films drops with the reduction of film thickness and crystallization (from f-C to A). Nanoindentation results at shallow penetrations were likely influenced by the surface roughness.

Finally, pop-in events observed in the load-displacement nanoindentation curves were related to dislocation mechanisms. The results also suggested that dislocation density increased with the film thickness.

Formatting of funding sources

This work was partly supported through grant ANR-16-CE08-0025, ANR NanoPiC from French National Research Agency.

CRediT authorship contribution statement

Stephania Kossman: Conceptualization, Methodology, Investigation, Formal analysis, Writing – original draft. **Arthur Hamieh:** Conceptualization, Methodology, Investigation, Formal analysis, Writing – original draft. **Freddy Ponchel:** Supervision. **Denis Rémiens:** Conceptualization, Methodology, Supervision, Writing – review & editing. **Maxence Bigerelle:** Supervision, Writing – review & editing.

Declaration of Competing Interest

The authors declare that they have no known competing financial interests or personal relationships that could have appeared to influence the work reported in this paper.

References

[1] I. Kanno, MEMS Piezoelectric, Ferroelectric thin films for MEMS applications, Jpn. J. Appl. Phys. 57 (2018), 040101, https://doi.org/10.7567/JJAP.57.040101.

[2] M.S. Vijaya, Piezoelectric Materials and Devices: Applications in Engineering and Medical Sciences, CRC Press, 2012.

[3] K. Shibata, R. Wang, T. Tou, J. Koruza, Applications of lead-free piezoelectric materials, MRS Bull. 43 (2018) 612–616, https://doi.org/10.1557/mrs.2018.180.

[4] EC, Directive 2002/95/EC of the European Parliament and of the Council of 27 January 2003 on the restriction of the use of certain hazardous substances in electrical and electronic equipment, 197, Official Journal of the European Union, 2012, pp. 38–71.

[5] Regulation (EC) No 1907/2006 of the European Parliament and of the Council of 18 December 2006 concerning the Registration, Evaluation, Authorisation and Restriction of Chemicals (REACH), establishing a European Chemicals Agency, amending Directive 1999/45/EC and repealing Council Regulation (EEC) No 793/93 and Commission Regulation (EC) No 1488/94 as well as Council Directive 76/769/EEC and Commission Directives 91/155/EEC, 93/67/EEC, 93/105/EC and 2000/21/EC, 2022, pp. 1–849, 396.

[6] S.-W. Zhang, Z. Zhou, J. Luo, J.-F. Li, Potassium-sodium-niobate-based thin films: lead free for micro-piezoelectrics, Annalen Der Physik 531 (2019), 1800525, https://doi.org/10.1002/andp.201800525.

[7] A. Hamieh, F. Ponchel, S. Barrau, D. Remiens, Synthesis of lead-free (Bi0,5Na0,5) TiO3 thin film by RF magnetron sputtering: impact of Na on the properties of film, Ferroelectrics 556 (2020) 79–86, https://doi.org/10.1080/00150193.2020.1713345.

[8] A. Hamieh, F. Ponchel, D. Remiens, Composition control of lead-free piezoelectric BNT thin ceramic films deposited by ex situ sputtering, J. Am. Ceram. Soc. 104 (2021) 4381–4388, https://doi.org/10.1111/jace.17890.

[9] R. Dittmer, W. Jo, K.G. Webber, J.L. Jones, J. Rödel, Local structure change evidenced by temperature-dependent elastic measurements: case study on Bi1/2Na1/2TiO3-based lead-free relaxor piezoceramics, J. Appl. Phys. 115 (2014), 084108, https://doi.org/10.1063/1.4866092.

[10] D.Q. Xiao, D.M. Lin, J.G. Zhu, P. Yu, Investigation on the design and synthesis of new systems of BNT-based lead-free piezoelectric ceramics, J. Electroceram. 16 (2006) 271–275, https://doi.org/10.1007/s10832-006-9863-7.

[11] Y.S. Sung, J.M. Kim, J.H. Cho, T.K. Song, M.H. Kim, H.H. Chong, T.G. Park, D. Do, S.S. Kim, Effects of K nonstoichiometry in (Bi0.5K0.5+x)TiO3 Ceramics, Integr. Ferroelectr 114 (2010) 92–99, https://doi.org/10.1080/10584587.2010.488190.

[12] Y.S. Sung, J.M. Kim, J.H. Cho, T.K. Song, M.H. Kim, T.G. Park, Effects of Bi nonstoichiometry in (Bi0.5+xNa)TiO3 ceramics, Appl. Phys. Lett. 98 (2011), 012902, https://doi.org/10.1063/1.3525370.

[13] B. Parija, T. Badapanda, P. Sahoo, M. Kar, P. Kumar, S. Panigrahi, Structural and electromechanical study of Bi0.5Na0.5TiO3-BaTiO3 solid-solutions, PAC 7 (2013) 73–80, https://doi.org/10.2298/PAC1302073P.

[14] T. Yu, K.-W. Kwok, H. Chan, Sol-gel derived lead-free piezoelectric Bi1/2Na1/2TiO3 thin film for MEMS applications, in: 2006 15th Ieee International Symposium on the Applications of Ferroelectrics, 2006, pp. 186–188, https://doi.org/10.1109/ISAF.2006.4387856.

[15] W. Sakamoto, N. Makino, B.-Y. Lee, T. Iijima, M. Moriya, T. Yogo, Influence of volatile element composition and Mn doping on the electrical properties of lead-free piezoelectric (Bi0.5Na0.5)TiO3 thin films, Sens. Actuator A Phys. 200 (2013) 60–67, https://doi.org/10.1016/j.sna.2012.10.006.

[16] S.A. Dargham, F. Ponchel, Y. Zaatar, J. Assaad, D. Remiens, D. Zaouk, Synthesis and characterization of BNT Thin Films prepared by Sol-gel method, Mater. Today: Proc. 3 (2016) 810–815, https://doi.org/10.1016/j.matpr.2016.02.013.
[17] S. Quignon, C. Soyer, D. Remiens, Synthesis and electrical properties of sputtered (Na0.5Bi0.5)TiO3 thin films on silicon substrate, J. Am. Ceram. Soc. 95 (2012) 3180–3184, https://doi.org/10.1111/j.1551-2916.2012.05285.x.
[18] K. Zhan, X.J. Zheng, J.F. Peng, Y.K. Zhu, H.B. Cheng, Effects of potassium content on the electrical and mechanical properties of (Na1-xKx)0.5Bi0.5TiO3 thin films, Ceram. Int. 41 (2015) 3474–3480, https://doi.org/10.1016/j.ceramint.2014.10.173.
[19] L. Xujun, P. Yong, G. Yueqiu, H. Renjie, L. Jiajia, X. Shuhong, Z. Yichun, G. Xingsen, Effects of niobium content on electrical and mechanical properties of (Na0.85K0.15)0.5Bi0.5Ti(1-x)NbxO3 thin films, J Mater Sci: Mater Electron. 25 (2014) 1416–1422, https://doi.org/10.1007/s10854-014-1744-2.
[20] K. Zhan, M. Su, H. Han, S.F. Xie, Y.K. Zhu, D. Wang, H.B. Cheng, X.Y. Wang, Effect of annealing temperature on piezoelectric and mechanical properties of (Bi0.5Na0.5)TiO3–(Bi0.5K0.5)TiO3–BaTiO3 thin films, Ceram. Int. 42 (2016) 1627–1632, https://doi.org/10.1016/j.ceramint.2015.09.114.
[21] Y. Li, S. Feng, W. Wu, F. Li, Temperature dependent mechanical property of PZT film: an investigation by nanoindentation, PLoS One 10 (2015), https://doi.org/10.1371/journal.pone.0116478.
[22] M. Detalle, D. Rémiens, Chemical and physical characterization of LaNiO3 thin films deposited by sputtering for top and bottom electrodes in ferroelectric structure, J. Cryst. Growth. 310 (2008) 3596–3603, https://doi.org/10.1016/j.jcrysgro.2008.04.053.
[23] R. Herdier, D. Jenkins, E. Dogheche, D. Rèmiens, M. Sulc, Laser Doppler vibrometry for evaluating the piezoelectric coefficient d33 on thin film, Rev. Sci. Instrum. 77 (2006), 093905, https://doi.org/10.1063/1.2349605.
[24] M. Pokorny, M. Sulc, R. Herdier, D. Remiens, E. Dogheche, D. Jenkins, Measurement methods for the d 33 coefficient of PZT thin films on silicon substrates: a comparison of double-beam laser interferometer (DBI) and single-beam laser vibrometer (LDV) techniques, Ferroelectrics 351 (2007) 122–130, https://doi.org/10.1080/00150190701354109.
[25] W.C. Oliver, G.M. Pharr, An improved technique for determining hardness and elastic modulus using load and displacement sensing indentation experiments, J. Mater. Res. 7 (1992) 1564–1583, https://doi.org/10.1557/JMR.1992.1564.
[26] W.C. Oliver, G.M. Pharr, Measurement of hardness and elastic modulus by instrumented indentation: Advances in understanding and refinements to methodology, J. Mater. Res. 19 (2004) 18, https://doi.org/10.1557/jmr.2004.19.1.3.
[27] P. Zaumseil, High-resolution characterization of the forbidden Si 200 and Si 222 reflections, J Appl Crystallogr 48 (2015) 528–532, https://doi.org/10.1107/S1600576715004732.
[28] V. Ion, F. Craciun, N.D. Scarisoreanu, A. Moldovan, A. Andrei, R. Birjega, C. Ghica, F. Di Pietrantonio, D. Cannata, M. Benetti, M. Dinescu, Impact of thickness variation on structural, dielectric and piezoelectric properties of (Ba,Ca)(Ti,Zr)O3 epitaxial thin films, Sci Rep. 8 (2018) 2056, https://doi.org/10.1038/s41598-018-20149-y.
[29] T. Haccart, E. Cattan, D. Remiens, Dielectric, ferroelectric and piezoelectric properties of sputtered PZT thin films on Si substrates: influence of film thickness and orientation, Semicond. Phys. Quantum Electron. Optoelectron. 5 (2002) 78–88.
[30] A.C. Fischer-Cripps, Nanoindentation, 3rd ed, Springer, New York, 2011.
[31] F. Pöhl, Pop-in behavior and elastic-to-plastic transition of polycrystalline pure iron during sharp nanoindentation, Sci. Rep. 9 (2019) 15350, https://doi.org/10.1038/s41598-019-51644-5.
[32] S. Kossman, M. Bigerelle, Pop-in identification in nanoindentation curves with deep learning algorithms, Materials 14 (2021) 7027, https://doi.org/10.3390/ma14227027.
[33] Š. Masys, V. Jonauskas, Elastic properties of rhombohedral, cubic, and monoclinic phases of LaNiO3 by first principles calculations, Comput. Mater. Sci. 108 (2015) 153–159, https://doi.org/10.1016/j.commatsci.2015.06.034.
[34] P. Delobelle, O. Guillon, E. Fribourg-Blanc, C. Soyer, E. Cattan, D. Rèmiens, True Young modulus of Pb(Zr,Ti)O3 films measured by nanoindentation, Appl. Phys. Lett. 85 (2004) 5185–5187, https://doi.org/10.1063/1.1827331.
[35] M. Qasmi, P. Delobelle, Influence of the average roughness Rms on the precision of the Young's modulus and hardness determination using nanoindentation technique with a Berkovich indenter, Surf. Coat. 201 (2006) 1191–1199, https://doi.org/10.1016/j.surfcoat.2006.01.058.
[36] Metallic Materials — Instrumented Indentation Test for Hardness and Materials Parameters — Part 1: Test method, ISO 14577-1, 2015.
[37] T. Coorevits, S. Kossman, D. Chicot, F. Hennebelle, A. Montagne, A. Iost, Virtual machine concept applied to uncertainties estimation in instrumented indentation testing, J. Mater. Res. 34 (2019) 2501–2516, https://doi.org/10.1557/jmr.2019.203.
[38] S. Kossman, D. Chicot, A. Iost, Indentation instrumentée multi-échelles appliquée à l'étude des matériaux massifs métalliques, Matériaux Tech. 105 (2017) 104, https://doi.org/10.1051/mattech/2017007.
[39] J. Menčík, M.V. Swain, Errors associated with depth-sensing microindentation tests, J. Mater. Res. 10 (1995) 1491–1501, https://doi.org/10.1557/JMR.1995.1491.
[40] K. Durst, M. Göken, H. Vehoff, Finite element study for nanoindentation measurements on two-phase materials, J. Mater. Res. 19 (2004) 85–93, https://doi.org/10.1557/jmr.2004.19.1.85.
[41] A. Ayrikyan, O. Prach, N.H. Khansur, S. Keller, S. Yasui, M. Itoh, O. Sakata, K. Durst, K.G. Webber, Investigation of residual stress in lead-free BNT-based ceramic/ceramic composites, Acta Mater 148 (2018) 432–441, https://doi.org/10.1016/j.actamat.2018.02.014.
[42] C.W. Huang, W. Ren, V.C. Nguyen, Z. Chen, J. Wang, T. Sritharan, L. Chen, Abnormal Poisson's ratio and Linear Compressibility in Perovskite Materials, Adv. Mater. 24 (2012) 4170–4174, https://doi.org/10.1002/adma.201104676.
[43] H. Nazeer, M.D. Nguyen, Ö.S. Sukas, G. Rijnders, L. Abelmann, M.C. Elwenspoek, Compositional dependence of the young's modulus and piezoelectric coefficient of (110)-oriented pulsed laser deposited PZT thin films, J Microelectromech Syst 24 (2015) 166–173, https://doi.org/10.1109/JMEMS.2014.2323476.
[44] P. Delobelle, G.S. Wang, E. Fribourg-Blanc, D. Remiens, Mechanical properties measured by nano-indentation of Pb(Zr, Ti)03 sol–gel films deposited on Pt and LaNi03 electrodes, Surf. Coat. 201 (2006) 3155–3162, https://doi.org/10.1016/j.surfcoat.2006.06.034.
[45] D. Wu, T.G. Nieh, Incipient plasticity and dislocation nucleation in body-centered cubic chromium, Mater. Sci. Eng. A. 609 (2014) 110–115, https://doi.org/10.1016/j.msea.2014.04.107.
[46] T.B. Britton, D. Randman, A.J. Wilkinson, Nanoindentation study of slip transfer phenomenon at grain boundaries, J. Mater. Res. 24 (2009) 607–615, https://doi.org/10.1557/jmr.2009.0088.
[47] S. Jiapeng, L. Cheng, J. Han, A. Ma, L. Fang, Nanoindentation induced deformation and pop-in events in a silicon crystal: molecular dynamics simulation and experiment, Sci. Rep. 7 (2017) 10282, https://doi.org/10.1038/s41598-017-11130-2.
[48] K. Fu, Y. Tang, L. Chang, Toughness assessment and fracture mechanism of brittle thin films under nano-indentation, in: L.M. Alves (Ed.), Fracture Mechanics - Properties, Patterns and Behaviours, InTech, 2016, https://doi.org/10.5772/64117.
[49] J.S. Field, M.V. Swain, R.D. Dukino, Determination of fracture toughness from the extra penetration produced by indentation-induced pop-in, J. Mater. Res. 18 (2003) 1412–1419, https://doi.org/10.1557/JMR.2003.0194.
[50] X. Fang, H. Bishara, K. Ding, H. Tsybenko, L. Porz, M. Höfling, E. Bruder, Y. Li, G. Dehm, K. Durst, Nanoindentation pop-in in oxides at room temperature: Dislocation activation or crack formation? J. Am. Ceram. Soc. 104 (2021) 4728–4741, https://doi.org/10.1111/jace.17806.
[51] S.-R. Jian, J.-Y. Juang, Indentation-induced mechanical deformation behaviors of AlN thin films deposited on c-plane sapphire, J. Nanomaterials. 2012 (36) (2012) 36, https://doi.org/10.1155/2012/914184.
[52] E. Navickas, Y. Chen, Q. Lu, W. Wallisch, T.M. Huber, J. Bernardi, M. Stöger-Pollach, G. Friedbacher, H. Hutter, B. Yildiz, J. Fleig, Dislocations accelerate oxygen ion diffusion in La0.8Sr0.2MnO3 epitaxial thin films, ACS Nano 11 (2017) 11475–11487, https://doi.org/10.1021/acsnano.7b06228.